Powder Technology 235 (2013) 540–549

Contents lists available at SciVerse ScienceDirect

Powder Technology

journal homepage: www.elsevier.com/locate/powtec

Effect of shear rate on aggregate size and structure in the process of aggregation and at steady state

Petra Bubakova, Martin Pivokonsky *, Petr Filip

Institute of Hydrodynamics, Academy of Sciences of the Czech Republic, Pod Patankou 5, 166 12 Prague 6, Czech Republic

ARTICLE INFO

Article history:
Received 7 June 2012
Received in revised form 29 October 2012
Accepted 10 November 2012
Available online 16 November 2012

Keywords:
Aggregation
Aggregate size
Fractal dimension
Shear rate
Steady state
Time evolution

ABSTRACT

The paper deals with the dependence of aggregate properties on the shear rate (G) in the aggregation process and at steady state. Natural raw water and ferric sulphate were aggregated in a Taylor–Couette reactor. The methods of image and fractal analysis were used to determine the aggregate size and structure. It was observed that at the early phase of aggregation, the aggregate growth rate is higher for lower shear rates. At $G \leq 150\ s^{-1}$, the time aggregation curve contains the local maximum before reaching the steady state. Moreover, the different extent of break-up and restructuring was proved for different values of shear rate. At $G \geq 200\ s^{-1}$, the aggregation curve misses the local extreme completely. It was found that with increasing shear rate ($G = 21.2–347.9\ s^{-1}$), the aggregates are smaller ($d = 1504–56\ \mu m$), more compact ($D_2 = 1.54–1.91$) and more regular ($D_{pf} = 1.37–1.10$). A relationship for the description of dependence of fractal dimension on the shear rate was also suggested.

1. Introduction

The processes of destabilization and aggregation are traditionally used to remove colloidal particles in water treatment. The purpose is to prepare aggregates of such properties (size, structure, shape, density, etc.) that are suitable for reaching the maximum effectiveness of following separation steps, such as sedimentation, filtration or flotation.

The formation of suspension includes the processes of *aggregation*, *break-up* and in some cases *restructuring* [1–5]. These processes can (but do not have to) proceed simultaneously and they depend on the balance between the hydrodynamic force F and the cohesive force J. The hydrodynamic force arises from a flow of fluid around a particle and is thus determined by the magnitude of the shear rate G, cross-sectional area of a particle A and dynamic viscosity of fluid μ. The cohesive force is given by the sum of all attractive forces acting between interacting particles (e.g. van der Waals, electrostatic or hydrophobic forces). It depends particularly on the particle (and/or reagent) composition and concentration and determines the strength of formed aggregates [1,4,6–8]. If the cohesive force prevails ($J > F$), aggregation occurs. If the hydrodynamic force prevails ($F > J$), aggregates are not formed at all or a break-up of already existing aggregates takes place. When these forces are approximately in equilibrium, the restructuring occurs.

When chemical conditions (type and concentration of particles and reagents, pH and overall water composition) are kept constant, the cohesive force between two primary particles does not change during the aggregation process. However, the hydrodynamics are influenced by the shear rate in the mixed volume which is not spatially (and temporally) constant at all and which depends on the geometry of the mixing tank and stirrer shape and speed (and temperature as well). This fact allows the already formed aggregates to be broken again when exposed to the regions with higher shear rates [8–13]. Nevertheless, the global/mean/average shear rate is still used for the characterization of hydrodynamics for practical reasons.

There are different perspectives on studying aggregate properties. First, it is the development of properties in time as the suspension is being formed (aggregation kinetics) and another, it is the description of aggregate properties at a steady state when they stabilize at some constant values. Both can be studied theoretically and/or experimentally.

The aggregation kinetics is theoretically studied with the use of population balance modelling based on the classical equation developed by Smoluchowski [14] which expresses the change of the number concentration of aggregates in time. This model assumes that only binary collisions between particles occur, the collision efficiency is 100%, colliding particles are spherical and of equal size, and neither aggregate break-up nor restructuring is considered. This expression has been modified by adding terms representing the aggregate break-up [15] and structure changes [3]. Population balances were then used by many other authors [3,5,13,16–19]. Experimental results that have been reported so far generally show two different trends of the development of aggregate size in time. In the first case, the aggregate size increases with time quite rapidly in the early stage of aggregation, and the growth slows down gradually until the steady state is reached [2,5,20–24]. In the other case, the aggregates grow to a maximum and then their size decreases again before a steady state is reached [3,9,11,12,18,25,26]. The reason for the appearance of such a peak in a size-time profile has not yet been satisfactorily

* Corresponding author. Tel.: +420 233 109 068; fax: +420 233 324 361.
E-mail address: pivo@ih.cas.cz (M. Pivokonsky).

0032-5910/$ – see front matter © 2012 Elsevier B.V. All rights reserved.
http://dx.doi.org/10.1016/j.powtec.2012.11.014

explained, although there are some suggestions that it might be the result of restructuring (break-up and re-aggregation) [11].

It has been reported up to now that the aggregate size at steady state decreases with increasing shear rate and a power function is often used for a description of this dependence [6,7,10,27–34]. The aggregate structure is described by means of different fractal dimensions which, in most cases, are calculated from the image analysis data [25,32,34–36] or light scattering data [2,5,8,11,23,24,37,38]. It follows from the published results that with increasing shear rate, aggregates become denser, more compact and less porous.

The paper deals with the dependence of the aggregate properties on the shear rate during the aggregation process and at a steady state. The aim of the paper is 1) to supplement existing knowledge of time evolution of aggregation process, especially with respect to processes of break-up and restructuring and 2) to suggest a new approach to the dependence of aggregate properties on the shear rate at a steady state. The relationship of aggregate properties and the shear rate was studied experimentally with the use of natural raw water and a hydrolyzing destabilization reagent, assuming action of other cohesive forces than just van der Waals and electrostatic. The aggregation was performed in a Taylor–Couette reactor, the flow conditions of which are well explored [5,24,35,39–45].

2. Materials and methods

2.1. Raw water and reaction conditions

The experiment used raw water from the Svihov reservoir (potable water source), Czech Republic. The tests were carried out during the winter period (January) when raw water quality was stable with the parameters given in Table 1. Ferric sulphate hydrate $Fe_2(SO_4)_3 \cdot 9H_2O$ (Analytika, Ltd., Czech Republic) served as coagulant. Its dose (3.98 mg l^{-1} of Fe) was optimized by standard jar tests. Thus, the formed aggregates consisted of the particles of impurities present in raw water as well as the particles of ferric hydroxide (coagulant). All laboratory tests were carried out at a temperature of 20 °C.

2.2. Taylor–Couette reactor and mixing conditions

The Taylor–Couette reactor was used as a mixing device. It consisted of a pair of concentric cylinders, with an inner rotating cylinder. The inner cylinder had a radius of $R_1 = 76$ mm and the outer had a radius of $R_2 = 85.5$ mm, which results in a gap width of $d = R_2 - R_1 = 9.5$ mm and radius ratio of $\eta = R_1/R_2 = 76/85.5 = 0.889$. The height of the cylinders was $H = 350$ mm resulting in the aspect ratio of $\Gamma = H/d = 350/9.5 = 36.8$.

Both cylinders were made of plexiglass (Umaplex, Perspex); the inner one was painted white, and served as a contrast background for the aggregates having an orange-brownish color. The outer cylinder was transparent and allowed the photographic imaging of the aggregation process. The inner cylinder was driven by a variable speed drive with a torque-meter. The hydrodynamic conditions in the Taylor–Couette reactor were characterised by the global shear rate $\overline{G}$ calculated according to the relationship as follows:

$$\overline{G} = \sqrt{\frac{P_i}{V\mu}} = \sqrt{\frac{\omega\ M}{V\mu}} = \sqrt{\frac{2\pi f M}{V\mu}}, \quad (1)$$

where P_i represents the power dissipated in the aggregation space, V is the volume of the aggregation space, μ is the dynamic viscosity of the fluid, ω is the angular velocity of inner cylinder rotation, M is the torque and f is the rotation frequency.

The flow regime in the gap between two cylinders is characterized by the Reynolds number

$$Re = \frac{\omega R_1 d}{\nu}, \quad (2)$$

where ω is the inner cylinder angular velocity, R_1 is the radius of the inner cylinder, $d = R_2 - R_1$ is the annular gap width, and ν is the kinematic viscosity.

For a fixed outer cylinder and Newtonian fluid, it is well known that as the angular velocity of the inner cylinder increases from rest, the flow undergoes a series of transitions: laminar Couette flow → laminar Taylor vortex flow → wavy vortex flow → modulated wavy vortex flow (→ weakly turbulent vortex flow) → turbulent vortex flow → turbulent flow [42]. These flow regimes can be characterised by the means of Reynolds number ratio $R = Re/Re_c$, where Re_c is the critical Reynolds number depending upon the specific geometry (i.e., the radius and aspect ratio) of the Taylor–Couette reactor used [44,45].

Table 2 shows the values of the global (mean) shear rate used in the experiment and corresponding angular velocities, Reynolds numbers and Reynolds number ratios. The value of Re_c for $\eta = 0.889$, $Re_c = 130.65$, was determined according to DiPrima et al. [41].

It follows from Table 2 and the literature that the flow regime in the Taylor–Couette reactor during the experiments varied from wavy vortex flow to turbulent vortex flow, transition at $R \sim 35$, and further, to fully developed turbulence, $R > 100$ [24,40,43–45].

2.3. Image analysis

The size of aggregates formed during the aggregation process in the Taylor–Couette reactor was determined by two-dimensional image analysis. This image processing technique has been developed to measure the aggregate size distribution in an aggregating suspension at any moment [32,34,46]. It is based on three steps:

1) Illuminating a slice of flow in the aggregation reactor with a laser light sheet (width = 1.2 ± 0.1 mm) generated by a laser diode (λ = 675 nm, power capacity 20 mW).
2) Recording images of the aggregate using a digital camera Pentax K20D (Asahi Co., Japan) with a Sigma AF 105/2.8 EX MACRO lens magnification 1:1 (Sigma Co., Japan).

Table 1
The quality of raw water.

Parameter	Value
T [°C]	3.6
pH [-]	7.2
Alkalinity [mmol l^{-1}]	1.09
Turbidity [NTU]	2.9
DOC [mg l^{-1}]	3.8
Fe [mg l^{-1}]	0.05
TSS [mg l^{-1}]	22.6

DOC — Dissolved Organic Carbon.
TSS — Total Suspended Solids.

Table 2
The values of global shear rate used in the experiment and corresponding angular velocities, Reynolds numbers and Reynolds number ratios.

G [s^{-1}]	ω [rad s^{-1}]	Re [−]	R [−]
21.2	2.50	1779	13.6
38.7	4.57	3247	24.9
58.9	6.95	4941	37.8
79.8	9.42	6695	51.2
102.3	12.08	8582	65.7
149.1	17.60	12509	95.7
202.2	23.87	16963	129.8
252.8	29.84	21208	162.3
300.5	35.48	25210	193.0
347.9	41.07	29187	223.4

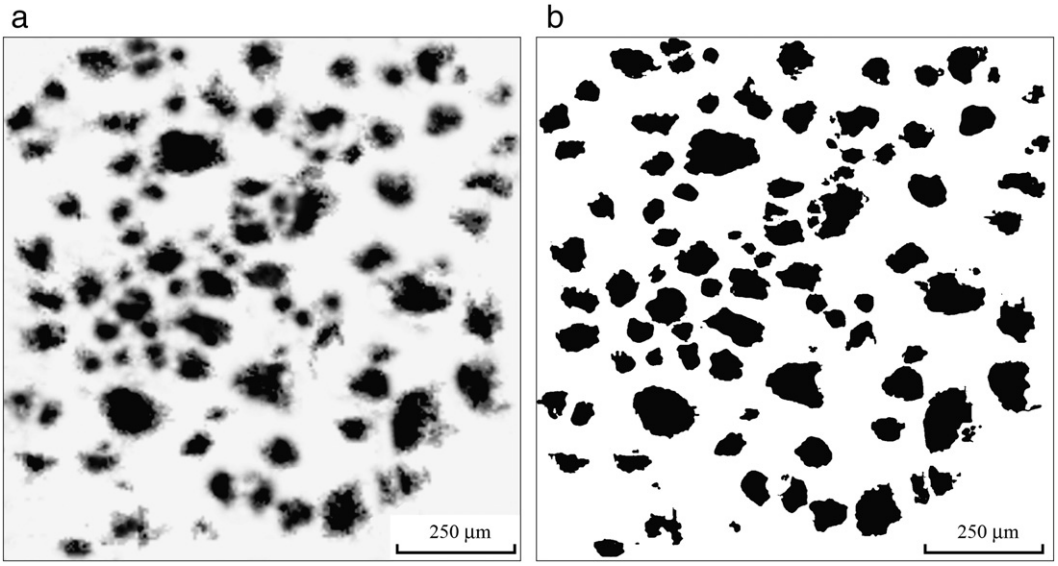

Fig. 1. (a) The bitmap image of aggregates at $G = 38.7\ s^{-1}$ and $t = 15$ min (steady state), (b) The corresponding binary image after thresholding.

3) Processing the images using image analysis software (Sigma Scan 5).

The digital images (22 × 14.6 mm) were taken after 1, 2, 3, 5, 7, 9, 12, 15, 20, 30, 45, and 60 minutes of aggregation in RAW format (4672 × 3104 pixels), which resulted in the pixel size of about 4.7 × 4.7 µm. In order to eliminate the digital background noise, only aggregates larger than 4 pixels (9.4 × 9.4 µm) were retained in the image analysis process. The images were converted from RAW format to BMP grey-scale format (the example is shown in Fig. 1a) and the thresholding was performed (Fig. 1b). Then, the Sigma Scan 5 software was used to calculate the projected area A and perimeter P of all imaged aggregates. The equivalent aggregate diameter d of each aggregate was calculated using the following equation:

$$d = \sqrt{4A/\pi} \tag{3}$$

The number of aggregates N in every single image was determined, and thus the average aggregate diameter d_{avr} could be calculated.

The main advantage of this size distribution measurement technique is that it is non-intrusive and therefore non-destructive. A detailed description of this technique was published in the previous paper [46].

2.4. Fractal analysis

A two-dimensional cluster fractal dimension was used to characterise the aggregate structure. It was calculated by the following equation from the slope of the log-log plot of the equivalent aggregate diameter d vs. the projected area of the aggregate A [36,47,48]

$$A \propto d^{D_2}. \tag{4}$$

For the calculation of the average value of fractal dimension, this study uses all aggregates in a given image, meeting the requirements from the previous section (aggregates larger than 4 pixels with well defined contour). The number of aggregates in each image differed depending on the shear rate used. The standard error was applied in determining the slopes from the regression lines. Densely packed (i.e. less porous) aggregates have a high fractal dimension, while a lower fractal dimension results from large, highly branched and loosely bound structures [36,37,49].

The geometry (or shape, regularity, surface morphology) of aggregates was evaluated with the use of the perimeter-based fractal dimension D_{pf} defined by the relationship between the measured perimeter P and the projected area A of the aggregate [5,38,49–52]

$$A \propto P^{2/D_{pf}}. \tag{5}$$

The values of D_{pf} were obtained (similarly as in the case of D_2) from the log-log plot of aggregate perimeter vs. projected area where they represented the slopes of fitted lines. The procedure of fractal dimension determination is illustrated in Fig. 2.

The value of D_{pf} varies between 1 (regular, spherical shape) and 2 (irregular, jagged surface, non-spherical shape). The interpretation of increasing D_{pf} is as follows: as the projected area A of the fractal aggregate increases, the aggregate perimeter P increases more rapidly than for Euclidean objects, so that the boundary becomes more convoluted [38,51].

3. Results and discussion

3.1. Time evolution of aggregate size and structure

The process of aggregation includes three sub-processes: aggregate growth, break-up and restructuring. Nevertheless, each of them can be involved in a different moment, or at a different shear rate, or does

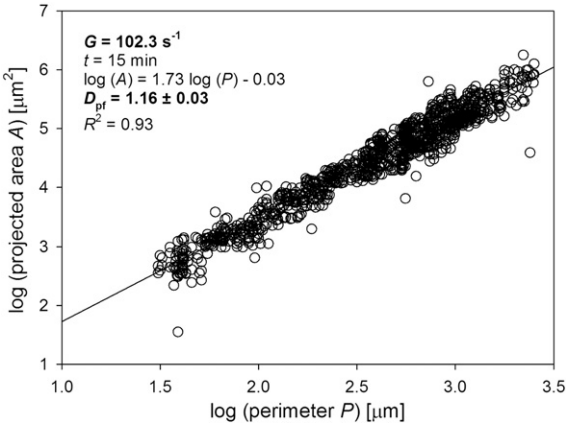

Fig. 2. Determination of perimeter-based fractal dimension (D_{pf}) of aggregates from image analysis measurements of aggregate projected area and perimeter — representative example for $G = 102.3\ s^{-1}$ and $t = 15$ min (steady state).

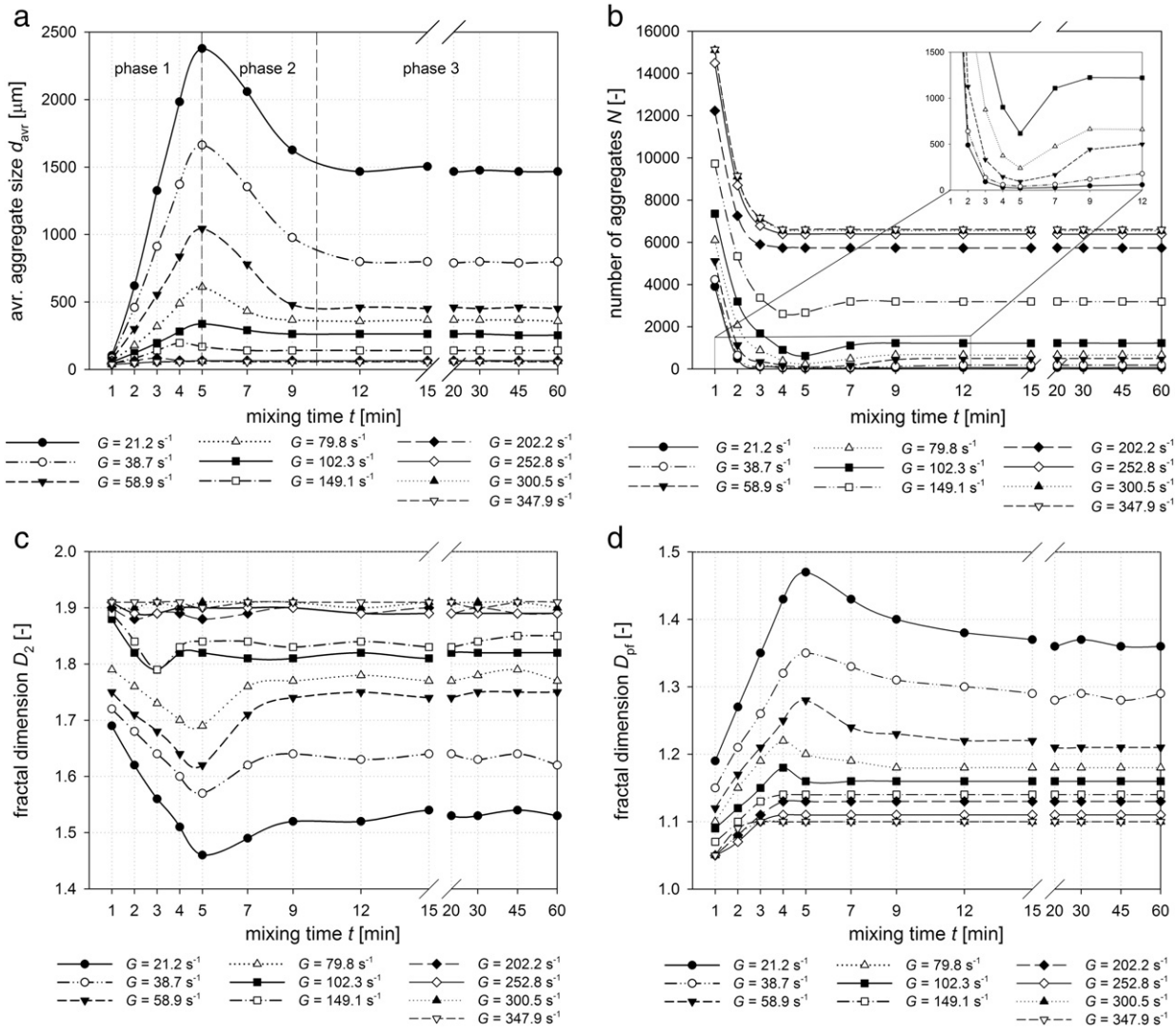

Fig. 3. a). Time evolution of the average aggregate size. b). Time evolution of the aggregate number. c). Time evolution of the fractal dimension D_2. d). Time evolution of the fractal dimension D_{pf}.

not have to be involved at all. Fig. 3a–d) show the time evolution of aggregate properties, namely, size (expressed by the average equivalent diameter d_{avr}), number (N), structure (expressed by the fractal dimension D_2) and shape (expressed by the fractal dimension D_{pf}), during the aggregation for a range of shear rates $G = 20–350\ s^{-1}$. For a better understanding, the time evolution can be divided into three phases, PI, PII and PIII (approximately illustrated in Fig. 3a): PI) aggregate growth, PII) aggregate break-up and/or restructuring, and PIII) steady state. What is happening in each from the mentioned phases at different shear rates is explained in the following text.

3.1.1. Phase I — aggregate growth

During this phase, the aggregate size and irregularity/jaggedness (D_{pf}) increases (Fig. 3a and d) and, simultaneously, the number and compactness (D_2) decreases (Fig. 3b and c). The decrease of D_2 is given by the connection of almost spherical primary particles with very high D_2 into an aggregate, necessarily containing spaces (or pores) and thus having lower D_2 (Fig. 3c). On the other hand, the D_{pf} increase is related to the increase of the aggregate perimeter (surface) due to the connection of primary particles (Fig. 3d).

For all shear rates used, there is a similar trend — an almost linear growth (in the case of size and D_{pf}) or decrease (number and D_2).

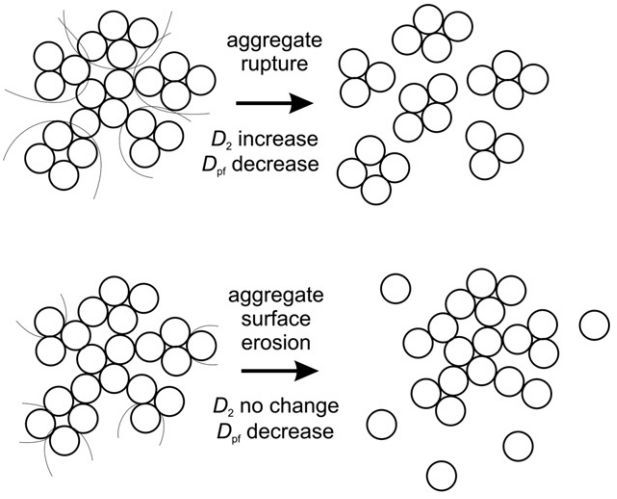

Fig. 4. Mechanisms of break-up and change in fractal dimensions. In the case of aggregate rupture, both size (parameter appearing in D_2 definition) and perimeter (parameter appearing in D_{pf} definition) changes significantly. In the case of aggregate surface erosion, only perimeter changes, and size remains almost constant.

Table 3
Summary of factors influencing the course of aggregation presented in selected literature.

Author	Type of particles	Primary particle size d_0	Solid volume fraction ϕ + particle number concentration n	Destabilization reagent type + dose D	Average (mean) shear rate G	Presence of maximum in the aggregation curve
De Boer et al. (1989)	polystyrene	$d_0 = 0.88$ μm	$\phi_1 = 2.4\times10^{-5}$ $\phi_2 = 4.8\times10^{-5}$ $\phi_3 = 7.2\times10^{-5}$ $\phi_4 = 1.2\times10^{-4}$	NaCl 467 mol/m^3	$G = 40, 95, 180$ s^{-1}	no
Williams et al. (1992)	silica slurry	$d_0 = 40$ μm (4–125 μm)	1% v/v 2% v/v 3% v/v 5% v/v	a) Zetag 92 (0.05 wt.%) + Magnafloc 1967 (0.5 wt.%) (1:1) b) Zetag 92	$G = 27$–190 s^{-1} rpm = 150–300 - effect of suspension viscosity !!!	yes — at all shear rates
Oles (1992)	polystyrene latex	$d_0 = 2.17$ μm	$\phi_1 = 10^{-6}$ $\phi_2 = 5\times10^{-6}$	NaCl 1.16 M	$G = 25, 50, 75, 100, 125, 150$ s^{-1}	no (possibly at $G = 25$ s^{-})
Spicer et al. (1996)	polystyrene	$d_0 = 0.87$ μm	$\phi = 1.4\times10^{-5}$ $n = 4\times10^7$ cm^{-3}	$Al_2(SO_4)_3.16H_2O$ $D = 10$ mg/l	$G = 15, 25, 50$ s^{-1}	yes — at $G = 25$ and 50 s^{-1} rather not — at $G = 15$ s^{-1} (disputable)
Spicer and Pratsinis (1996)	polystyrene	$d_0 = 0.87$ μm	$\phi_1 = 8.3\times10^{-5}$ $\phi_2 = 2.1\times10^{-5}$	$Al_2(SO_4)_3.16H_2O$ $D_1 = 4.3$ mg/l $D_2 = 10.7$ mg/l $D_3 = 32$ mg/l	$G = 63, 95, 129$ s^{-1}	not clearly distinguishable — more likely no
Flesch et al. (1999)	polystyrene	$d_0 = 0.87$ μm	$\phi = 1.4\times10^{-5}$ $n = 4\times10^7$ cm^{-3}	$Al_2(SO_4)_3.16H_2O$ $D = 10$ mg/l	$G = 50, 100, 150$ s^{-1}	no
Selomulya et al. (2001)	latex	$d_0 = 380$ nm	$\phi = 3.8\times10^{-5}$ $n = 1.25\times10^9$ cm^{-3}	KNO_3 D = N/A	$G = 16, 32, 40, 64, 80, 100$ s^{-1}	no — at $G = 16, 32, 40$ s^{-1} yes — at $G = 64, 80, 100$ s^{-}
Selomulya et al. (2002)	polystyrene latex	$d_{01} = 60$ nm $d_{02} = 380$ nm $d_{03} = 810$ nm	$\phi_1 = 3.83\times10^{-6}$ $\phi_2 = 3.74\times10^{-5}$ $\phi_3 = 3.76\times10^{-4}$ $n_1 = 3.4\times10^{10}$ cm^{-3} $n_1 = 1.3\times10^9$ cm^{-3} $n_1 = 1.4\times10^8$ cm^{-3}	$MgCl_2$ 0.05 M	$G = 32, 64, 100, 330$ (246) s^{-1}	yes — at $d_0 = 60$ and 380 nm and $G = 32, 64, 100$ s^{-1} and at $d_0 = 810$ nm and $G = 32$ s^{-1}
Rahmani et al. (2003)	asphaltene	N/A	$\phi = 3.38$–10.81×10^{-6}	–	$G = 1.2, 2.5, 3.8, 8.4, 12.7$ s^{-1}	yes — at $G = 2.5$ s^{-1} and $\phi = 8.6\times10^{-6}$ no — at $G = 2.5$ s^{-1} and $\phi = 4.43$ and 3.38×10^{-6} yes — at $\phi = 10.81\times10^{-6}$ and $G = 1.2, 2.5, 3.8, 8.4$ s^{-1} no — at $\phi = 10.81\times10^{-6}$ and $G = 12.7$ s^{-1}
Hopkins and Ducoste (2003)	kaolin	$d_0 < 1$ μm	50 mg/l 100 mg/l	$Al_2(SO_4)_3.16H_2O$ D = cca 10 mg/l	$G = 40, 50, 70, 90$ s^{-1}	no — at $G < 70$ s^{-1} yes — at $G \geq 70$ s^{-1}
Prat and Ducoste (2006)	clay	$d_0 = 1$ μm	100 mg/l	N/A	$G = 40, 70, 90, 150$ s^{-1}	no — at $G < 70$ s^{-1} yes — at $G \geq 70$ s^{-1}
Mutl et al. (2006)	natural water with NOM	N/A	N/A	$FeCl_3.6H_2O$ $D = 30$ mg/l	$G = 40, 60, 80, 100, 150, 200, 250, 300, 350$ s^{-1}	no — at $G > 100$ s^{-1} yes — at $G \leq 100$ s^{-1}
Heath et al. (2006)	calcite	$d_{01} = 2.36$ μm $d_{02} = 3.47$ μm $d_{03} = 6.59$ μm $d_{04} = 15.08$ μm $d_{05} = 24.26$ μm	1.23 % v/v 2.46 % v/v 3.69 % v/v 4.92 % v/v 6.15 % v/v	30% anionic acrylate-acrylamide copolymer $D_1 = 5$ g/t $D_2 = 10$ g/t $D_3 = 20$ g/t $D_4 = 40$ g/t $D_5 = 80$ g/t	$G = 9$–944.1 s^{-1}	yes — under all conditions (although some disputable exceptions can exist)
Soos et al. (2007)	latex	N/A	$\phi_1 = 3.754\times10^{-4}$ $\phi_2 = 3.937\times10^{-4}$ $\phi_3 = 7.877\times10^{-4}$	NaCl 1.45 M	$G = 34.96, 71.69$ s^{-1}	no
Ehrl et al. (2008)	sulfate polystyrene latex	$d_{01} = 120$ nm $d_{02} = 420$ nm	$\phi = 2\times10^{-5}$	$Al(NO_3)_3$ 30 ml (20% w/w) in 2.5 l	$G = 106, 287, 517, 1097$ s^{-1}	no
Ehrl et al. (2009)	sulfate polystyrene latex	$d_{01} = 120$ nm $d_{02} = 420$ nm $d_{03} = 810$ nm	$\phi_1 = 1\times10^{-5}$ $\phi_2 = 2\times10^{-5}$	$Al(NO_3)_3$ 30 ml (20% w/w) in 2.5 l	$G = 108$–1353 s^{-1}	no
Ehrl et al. (2010)	sulfate polystyrene latex	$d_0 = 600$ nm	$\phi = 2\times10^{-5}$	$Al(NO_3)_3$ 30 ml (20% w/w) in a) 1.35 l, b) 1.50 l, c) 1.99 l, d) 2.57 l	N/A rpm = 250, 362, 544, 718, 988, 1260	no

N/A = not available.

These observations are in agreement with other authors' research [3,9,13,17,51], although some others have reported that the growth of aggregate size is exponential [2,3,20,24,53]. The difference in the course of floc growth in the early phase of aggregation (linear vs. exponential trend) is caused by the different primary particle size due to the variation of the relative importance of Brownian aggregation with respect to shear aggregation [23].

Fig. 3a) also shows that the lower the shear rate is, the faster the aggregate size increases. This is caused by the fact that despite the lower collision rate, the collision efficiency increases with decreasing shear rate [2,7,11].

3.1.2. Phase II — break-up and/or restructuring

At low shear rates ($G = 20$ and 40 s^{-1}), there is a significant change in the aggregate size, but relatively low change in the number of aggregates. At the same time, the fractal dimensions D_2 and D_{pf} change as well. This implies that there is very little aggregate break-up and the restructuring predominates considerably.

At medium shear rates ($G = 60$ and 80 s^{-1}), the size, number and both fractal dimensions change, which leads to a conclusion that both restructuring and break-up take place. The break-up mechanism is probably the rupture of existing aggregates into smaller compact pieces rather than the primary particle erosion from the aggregate surface (schematically illustrated in Fig. 4), because both D_2 and D_{pf} fractal dimensions change significantly.

At higher shear rates ($G = 100$ and 150 s^{-1}), there is a big change in size and number. Therefore, it is assumed that the break-up is employed to the largest extent in these cases. Contrary to the previous shear rates, the erosion from the aggregate surface (Fig. 4) is the likely break-up mechanism, because although the D_{pf} fractal dimension changes, the change in D_2 is almost imperceptible.

At very high shear rates ($G \geq 200$ s^{-1}), phase II is completely absent and the aggregation curve misses the local extreme. There is no change of any property and the system reaches phase III (steady state) right after phase I. Thus, at such high shear rates, small and compact aggregates are formed directly and their break-up or restructuring does not occur at all. The possible explanation is that at very high shear rates, the distribution of flow rate is more uniform (there are smaller differences in shear rates at different parts of the mixed volume) than at low shear rates, and aggregates are not allowed to grow large enough to be subject to break-up.

Some authors [8–13] have suggested that the reduction in the aggregate size following a maximum value (in the case of low shear rates) was the consequence of break-up mechanisms (primary particle erosion from the aggregate surface or rupture of existing aggregates) due to the spatial differences in the shear rate in the mixing tank. Selomulya et al. [3] showed that this maximum value with the subsequent size reduction is accompanied by the changes in a structure (described by the means of fractal dimension), which supports the idea of aggregate restructuring —more compact arrangement of primary particles in aggregate results in the smaller aggregate size. The results presented in this paper confirm both ideas. Moreover, they suggest under what conditions each phenomenon (break-up and/or restructuring) occurs.

It is necessary to state that the course of aggregation, namely the presence of the local extreme in the aggregation curve, does not depend solely on the magnitude of the shear rate. According to population balance theory based on Smoluchowski [14], extended and modified by the others [3,5,16,19,21,54–58], the course of aggregation depends on the primary particle number N (particle concentration, solid volume fraction) and orthokinetic collision rate coefficient k_{ij} which depends on shear rate G and size of primary particles d_0. Table 3 shows the summary of these factors used in the literature and gives information about the shape of the aggregation curve, i.e. occurrence of the local maximum (peak). It is evident that some of these results are contrary to each other and it is almost impossible to draw any conclusion from such various results.

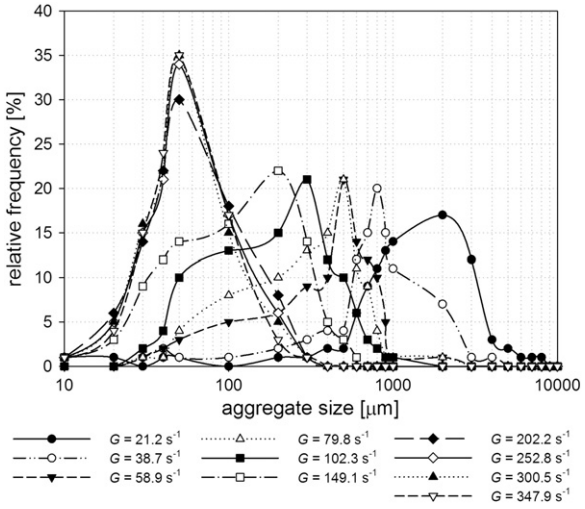

Fig. 5. Aggregate size distribution at different shear rates.

The variety of results can be given by the fact that some researchers might finish the measurement before the steady state was reached and as such, they could not observe the peak (maximum) (as suggested by Prat and Ducoste [13]).

3.1.3. Phase III — steady state

The phase of steady state, when the properties of aggregates change no more, is reached at all shear rates; nevertheless, it is reached earlier at higher G. The reason is that the collision rate coefficient (k_{ij}) for orthokinetic aggregation is directly proportional to the shear rate as stated before in the discussion of phase I. With increasing shear rate, the collision frequency increases together with break-up, which leads to the acceleration of aggregation and fragmentation [2,8,59]. The aggregate properties at steady state are discussed in the next Section (3.2).

It is needed to note that the time position of individual phases is different for different shear rates. For $G = 20$–100 s^{-1}, the turn from one phase to another takes place later (PI–PII — 5 min; PII–PIII — circa 10 min) than for $G = 150$ s^{-1} (PI-PII — 4 min; PII-PIII — 7 min) and for $G = 200$–350 s^{-1} (PI–PIII — 3 min; PII is completely missing). In the ranges of $G = 20$–100 s^{-1} and $G = 200$–350 s^{-1}, there can be also differences in times of phase turns which cannot be unfortunately observed because of not enough detailed (or too long) time interval of

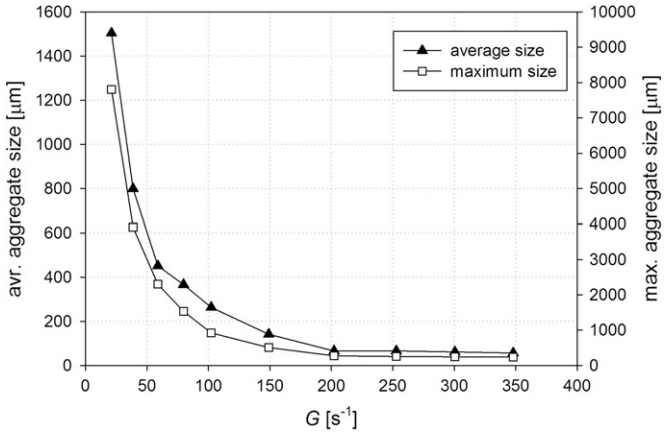

Fig. 6. Average and maximum aggregate sizes for different values of shear rate.

taking images. The explanation of this phenomenon was already given several lines above: the collision rate coefficient for orthokinetic aggregation is directly proportional to the shear rate, thus the processes of aggregation, break-up and restructuring can proceed faster at higher shear rates and time shift of individual phases occurs.

3.2. Aggregate size and structure at steady state

The aggregate properties at steady state were evaluated after 15 minutes of aggregation in the Taylor–Couette reactor.

From the image analysis, the aggregate size distribution recognized as log-normal was determined (Fig. 5). Generally, it can be concluded that the aggregate size distribution is narrower with increasing G value. The suspension with heterogeneous aggregate size distribution homogenizes itself due to increasing hydrodynamic force. At low G values, considerably large aggregates form; but smaller aggregates occur simultaneously in the system. For example, at shear rate $G = 21.2\ s^{-1}$, there is the greatest variability in formed aggregates — from circa 400 up to 5000 microns. On the contrary, at the highest shear rates (about 300 s^{-1}) aggregates only from circa 10 to 200 microns are present. Furthermore, the aggregate size distribution is practically identical at shear rates $G \geq 200\ s^{-1}$.

From the aggregate size distribution, characteristic aggregate length scales can be defined: the average aggregate diameter d_{avr}, maximum aggregate diameter d_{max} and most probable aggregate diameter d_{mp} (corresponding to the top of the peak of the size distribution curve) [10]. Fig. 6 shows the average and maximum aggregate sizes for different values of shear rate. In the first part of the curve (small shear rates, up to circa 80 s^{-1}), small increase of the shear rate produces big decrease of aggregate size. On the other hand, when the shear rate is increased above $G > 200\ s^{-1}$, the aggregate size changes only slightly. The trend of the average and maximum aggregate size is very similar. However, at shear rates in the interval 60–200 s^{-1}, a deviation is observed.

The properties of aggregates at steady state depend on the mixing intensity expressed by the *shear rate* (i.e. the hydrodynamic force) and the *aggregate strength* (i.e. the cohesive force). The aggregate strength is given by the character of interactions between the primary particles; the solid volume fraction or number concentration and size of primary particles; and the arrangement of primary particles in an aggregate [24,60]. The aggregate strength determines the extent of aggregate break-up. On the basis of these statements, a relationship between the maximum/average stable aggregate size and the average shear rate was derived [6,7,10,27–34]

$$d_{avr/max} = C\varepsilon^{-\gamma} = CG^{-2\gamma}, \tag{6}$$

where C and γ are aggregate strength constants for given system and conditions comprising all parameters mentioned above, i.e. type and magnitude of interactions, size and number of primary particles, etc., and possibly the density and viscosity of water or suspension. The mentioned expression is a decreasing power function which is displayed as a linear one when plotted in a logarithmic scale (log-log plot) [7,30–34].

Nevertheless, the measured data showed that when plotted in a log-log plot, there are two regions where Eq. (6) can be applied, however with the different numerical values of the parameters C and γ, and an intermediate region between them (Fig. 7a). Such an apparent division of the whole range of shear rates into these three regions

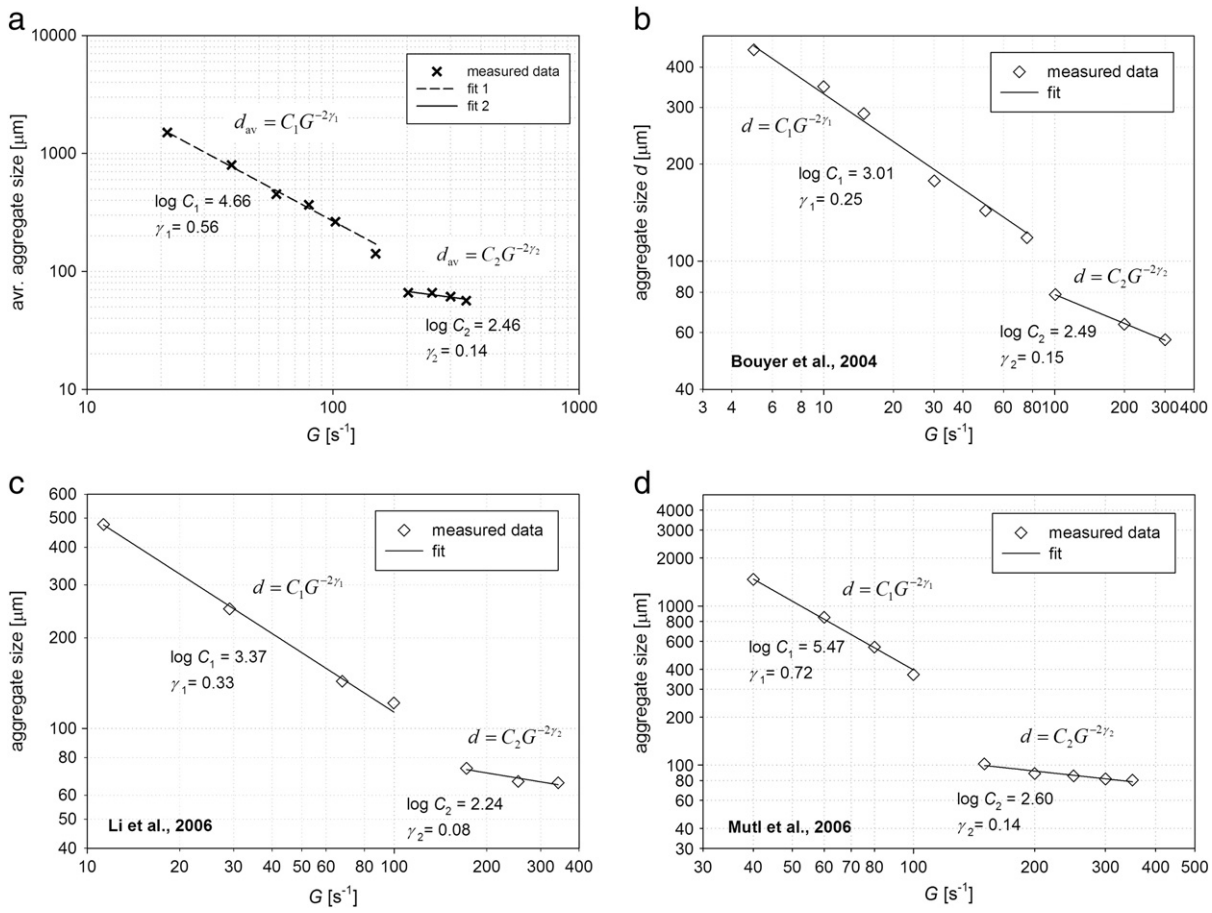

Fig. 7. a). Present data. b). Data measured by Bouyer et al. (2004). The aggregate size is influenced by using the aluminium coagulant. c). Data measured by Li et al. (2006). The aggregate size is influenced by using the aluminium coagulant. d). Data measured by Mutl et al. (2006). The aggregate size is influenced by using the ferric coagulant.

may lead to a consideration that they correspond to the following characterization:

1) First region, where G values are low and cohesion forces dominate the hydrodynamic ones ($J>F$);
2) Second (intermediate) region, where both forces are balanced ($J\sim F$);
3) Third region, where G values are high and hydrodynamic forces dominate the cohesion ones ($J<F$).

This implies an introduction of two pairs of adjustable parameters C and γ (C_1, γ_1; C_2, γ_2) corresponding to the regions where one of the two forces dominates (Fig. 7a). The result when an application of Eq. (6) is carried out separately is depicted also for the data of some other authors (Fig. 7b–d).

As the data measured and published in the literature do not cover all three regions sufficiently what concerns their density, it is not possible to determine (or propose) the smooth passage in the intermediate region connecting two linear segments (in a logarithmic scale) corresponding to first and third regions. Nevertheless, the indices of determination indicate a suitability of modelling in separate regions because in this case the correlation between the experimental data in the individual segments (in a logarithmic scale) is much better than that if the only curve is used throughout the whole region measured.

For the relationship between aggregate size, strength and applied shear rate, Eq. (6) has been widely used for a long time. However, with a development of using fractal analysis for characterizing the aggregate structure, it suggests itself to relate the aggregate strength and shear rate to the aggregate structure, i.e. density (or compactness) and porosity, often expressed by the means of the fractal dimension. Fig. 8a) and b) show the D_2 and D_{pf} fractal dimensions of aggregates formed at different shear rates, respectively.

For applied shear rates, the D_2 fractal dimension was found to range from 1.54 to 1.91 (Fig. 8a). It became higher with increasing shear rate, indicating that the aggregates became less porous and more compact [36,48,49]. If compared with Fig. 6, it can be seen that the fractal dimension increases (approaches Euclidean dimension) for smaller aggregates, which is in agreement with the work of Maggi et al. [61].

The D_{pf} fractal dimension generally represents the shape (or regularity) of an aggregate. The more it approaches the value of 1, the more regular the aggregates are. Our measurements showed that D_{pf} decreased from 1.37 to 1.10 with increasing G value (Fig. 8b). At higher shear rates, the D_{pf} values are lower, which indicates more regular aggregates. In contrast, at the low shear rates, the D_{pf} values are higher, which means the aggregates are more jagged on the surface with irregular shape.

As it was mentioned, an effort to find a relationship between fractal dimensions and shear rate was made. Fractal dimensions D_2 and D_{pf} attain the values between 1 and 2 (classical Euclidean dimensions) as follows from their definitions. As these fractal dimensions are 'symmetrical', i.e. an increment added to one (one-dimensional Euclidean dimension) in the case of D_{pf} should be equal to an increment subtracted from two (two-dimensional Euclidean dimension) in the case of D_2, the following expressions for evaluating the fractal dimensions D_{pf} and D_2 are proposed

$$D_{pf} = 1.5-(c_1 + k_1 \tanh(k_2 G + c_2)), \quad (7)$$

$$D_2 = 1.5 + (c_1 + k_1 \tanh(k_2 G + c_2)), \quad (8)$$

where the individual parameters attain (for both curves) the common values: $c_1 = -0.14$, $k_1 = 0.53$, $k_2 = 0.015$ and $c_2 = 0.1$.

A comparison between proposed and experimental values of fractal dimensions is illustrated in Fig. 8a) and b). The presented fits give a good result with $R^2 = 0.960$ for D_2 and $R^2 = 0.984$ for D_{pf}. It can be seen that the fitted curves describe the measured data quite accurately, mean deviation of the data from the proposed curves attain 1.7 % and 1.4 % for D_2 and D_{pf}, respectively. It is possible that the method of measurement and calculation of fractal dimension can influence the dependence found.

4. Conclusions

In this paper, the effect of shear rate on the aggregate size and structure was studied from two points of view; firstly, it was the course of the aggregation process in time and secondly, there were aggregate properties at a steady state. The presented results lead to the following conclusions:

- At the early phase of aggregation, the aggregate growth rate is higher for lower shear rates.
- At $G \leq 150\ s^{-1}$, the time aggregation curve contains the local extreme before reaching the steady state.
  - At $G = 20$ and $40\ s^{-1}$, there is very little aggregate break-up and the restructuring predominates considerably.
  - At $G = 60$ and $80\ s^{-1}$, both restructuring and break-up take place; in case of break-up, the mechanism of rupture of existing aggregates into smaller compact pieces happens.
  - At $G = 100$ and $150\ s^{-1}$, the break-up is employed to the largest extent. Contrary to the previous shear rates, the erosion from the aggregate surface would be the likely break-up mechanism.
- At $G \geq 200\ s^{-1}$, the aggregation curve misses the local extreme. There is no change of any property, and the system reaches steady state right after the growth phase. Break-up or restructuring does not occur at all from the global point of view.
- Two regions in a log-log plot of size vs. shear rate dependence,

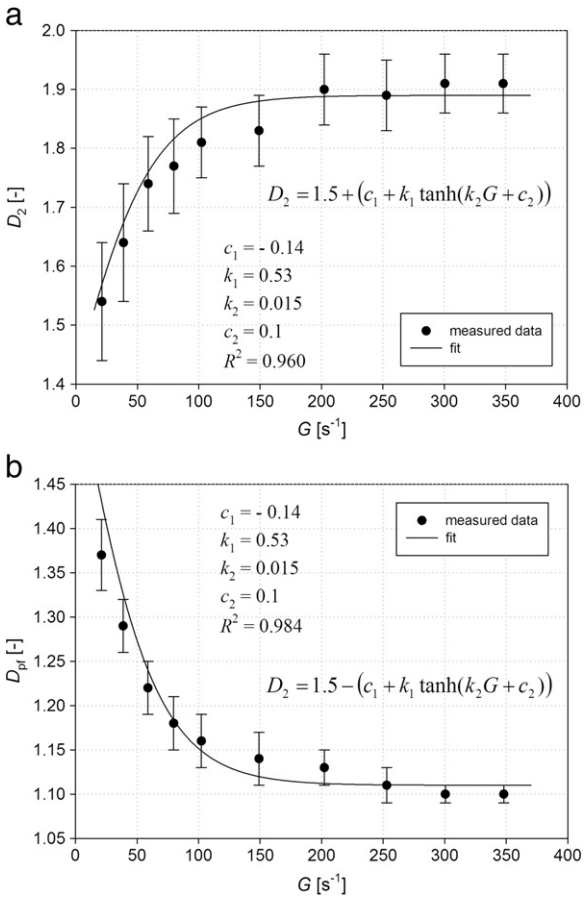

Fig. 8. a). The dependence of D_2 fractal dimension on the shear rate at steady state — Error bars indicate the standard deviation of D_2 values. b). The dependence of D_{pf} fractal dimension on the shear rate at steady state — Error bars indicate the standard deviation of D_{pf} values.

where the Equation $d_{avr/max} = CG^{-2\gamma}$ can be applied with different C and γ values, were observed. They can represent the areas of prevailing adhesion or hydrodynamic forces, respectively. However, the intermediate region between them still needs to be explored in a greater detail.

- A relationship for the description of dependence of fractal dimension on the shear rate was suggested.
- It was observed that with increasing shear rate, the aggregates are smaller, more compact and more regular. For $G = 21.2–347.9\ s^{-1}$, the average aggregate size ranged from 1504 to 56 μm, the D_2 fractal dimension was found to range from 1.54 to 1.91 and the D_{pf} fractal dimension decreased from 1.37 to 1.10.

Acknowledgements

This research project was funded by the Czech Science Foundation under project no. P105/11/0247.

References

[1] R.C. Sonntag, W.B. Russel, Structure and break-up of flocs subjected to fluid stresses: II Theory, Journal of Colloid and Interface Science 115 (2) (1987) 378–389.
[2] V. Oles, Shear-induced aggregation and breakup of polystyrene latex particles, Journal of Colloid and Interface Science 154 (2) (1992) 351–358.
[3] C. Selomulya, G. Bushell, R. Amal, T.D. Waite, Understanding the role of restructuring in flocculation: The application of a population balance model, Chemical Engineering Science 58 (2) (2003) 327–338.
[4] P. Jarvis, B. Jefferson, J. Gregory, S.A. Parsons, A review of floc strength and breakage, Water Research 39 (14) (2005) 3121–3137.
[5] M. Soos, L. Wang, R.O. Fox, J. Sefcik, M. Morbidelli, Population balance modeling of aggregation and breakage in turbulent Taylor–Couette flow, Journal of Colloid and Interface Science 307 (2) (2007) 433–446.
[6] N. Tambo, H. Hozumi, Physical characteristics of flocs — II. Strength of floc, Water Research 13 (5) (1979) 421–427.
[7] R.J. Francois, Strength of aluminium hydroxide flocs, Water Research 21 (9) (1987) 1023–1030.
[8] P.T. Spicer, S.E. Pratsinis, Shear-induced flocculation: The evolution of floc structure and the shape of the size distribution at steady state, Water Research 30 (5) (1996) 1049–1056.
[9] R.A. Williams, S.J. Peng, A. Naylor, In situ measurement of particle aggregation and breakage kinetics in a concentrated suspension, Powder Technology 73 (1) (1992) 75–83.
[10] D. Bouyer, A. Liné, A. Cockx, Z. Do-Quang, Experimental analysis of floc size distribution and hydrodynamics in a jar-test, Transactions of IchemE 79 (Part A) (2001) 1017–1024.
[11] C. Selomulya, R. Amal, G.C. Bushell, D. Waite, Evidence of shear rate dependence on restructuring and breakup of latex aggregates, Journal of Colloid and Interface Science 236 (1) (2001) 67–77.
[12] D.C. Hopkins, J.J. Ducoste, Characterizing flocculation under heterogeneous turbulence, Journal of Colloid and Interface Science 264 (1) (2003) 184–194.
[13] O.P. Prat, J.J. Ducoste, Modeling spatial distribution of floc size in turbulent processes using the quadrature method of moment and computational fluid dynamics, Chemical Engineering Science 61 (1) (2006) 75–86.
[14] M. Smoluchowski, Versuch einer Mathematischen Theorie der Koagulationskinetik Kolloider Lösungen, Zeitschrift für Physikalische Chemie 92 (2) (1917) 129–168.
[15] M.J. Hounslow, R.L. Ryall, V.R. Marshall, A discretized population balance for nucleation, growth, and aggregation, AICHE Journal 34 (11) (1988) 1821–1832.
[16] C.A. Biggs, P.A. Lant, Modelling activated sludge flocculation using population balances, Powder Technology 124 (3) (2002) 201–211.
[17] A.R. Heath, P.T.L. Koh, Combined population balance and CFD modelling of particle aggregation by polymeric flocculant, in: Proc. Third International Conference on CFD in the Minerals and Process Industries, CSIRO, 10-12 December, Melbourne, Australia, 2003, pp. 339–344.
[18] N.H.G. Rahmani, J.H. Masliyah, T. Dabros, Characterization of asphaltenes aggregation and fragmentation in a shear field, AICHE Journal 49 (7) (2003) 1645–1655.
[19] I. Nopens, D. Beheydt, P.A. Vanrolleghem, Comparison and pitfalls of different discretised solution methods for population balance models: a simulation study, Computers and Chemical Engineering 29 (2) (2005) 367–377.
[20] G.B.J. De Boer, G.F.M. Hoedemakers, D. Thoenes, Coagulation in turbulent flow. Part II, Chemical Engineering Research and Design 67 (3) (1989) 308–315.
[21] J.C. Flesch, P.T. Spicer, S.E. Pratsinis, Laminar and turbulent shear-induced flocculation of fractal aggregates, AICHE Journal 45 (5) (1999) 1114–1124.
[22] L. Ehrl, M. Soos, M. Morbidelli, Dependence of aggregate strength, structure, and light scattering properties on primary particle size under turbulent conditions in stirred tanks, Langmuir 24 (7) (2008) 3070–3081.
[23] L. Ehrl, M. Soos, M. Morbidelli, M.U. Bäbler, Dependence of initial cluster aggregation kinetics on shear rate for particles of different sizes under turbulence, AICHE Journal 55 (12) (2009) 3076–3087.
[24] L. Ehrl, M. Soos, H. Wu, M. Morbidelli, Effect of flow field heterogeneity in coagulators on aggregate size and structure, AICHE Journal 56 (10) (2010) 2573–2587.
[25] S. Mutl, P. Polasek, M. Pivokonsky, O. Kloucek, The influence of G and T on the course of aggregation in treatment of medium polluted surface water, Water Science and Technology: Water Supply 6 (1) (2006) 39–48.
[26] A.R. Heath, P.A. Bahri, P.D. Fawell, J.B. Farrow, Polymer flocculation of calcite: Experimental results from turbulent pipe flow, AICHE Journal 52 (4) (2006) 1547–5905.
[27] Y. Argaman, W.J. Kaufman, Turbulence and Flocculation, Journal of the Sanitary Engineering Division 96 (2) (1970) 223–241.
[28] D.S. Parker, W.J. Kaufman, D. Jenkins, Floc breakup in turbulent flocculation processes, Journal of the Sanitary Engineering Division 98 (1) (1972) 79–99.
[29] M. Sakurai, Y. Harano, Flocculation in microcellulose-aluminium sulphate disperse system, International Chemical Engineering 22 (1) (1982) 116–124.
[30] K. Mühle, Floc stability in laminar and turbulent flow, in: B. Dobias (Ed.), Coagulation and Flocculation, Marcel Dekker, New York, 1993, pp. 355–390.
[31] D.H. Bache, E.R. Rasool, D. Moffat, F.J. McGilligan, On the strength and character of alumino-humic flocs, Water Science and Technology 40 (9) (1999) 81–88.
[32] D. Bouyer, A. Liné, Z. Do-Quang, Experimental analysis of floc size distribution under different hydrodynamics in a mixing tank, AICHE Journal 50 (9) (2004) 2064–2081.
[33] T. Serra, J. Colomer, B.E. Logan, Efficiency of different shear devices on flocculation, Water Research 42 (2008) 1113–1121.
[34] M. Pivokonsky, P. Bubakova, L. Pivokonska, The effect of global velocity gradient on the character and filterability of aggregates formed during the coagulation/flocculation process, Environmental Technology 32 (12) (2011) 1355–1366.
[35] C. Coufort, D. Bouyer, A. Line, Flocculation related to local hydrodynamics in Taylor–Couette reactor and in a jar, Chemical Engineering Science 60 (8–9) (2005) 2179–2192.
[36] R.K. Chakraborti, K.H. Garner, J. Kaur, F.J. Atkinson, In situ analysis of flocs, Journal of Water Supply: Research and Technology-AQUA 56 (1) (2007) 1–11.
[37] T. Li, Z. Zhu, D. Wang, Ch. Yao, H. Tang, Characterization of floc size, strength and structure under various coagulation mechanisms, Powder Technology 168 (2) (2006) 104–110.
[38] M. Soos, A.S. Moussa, L. Ehrl, J. Sefcik, H. Wu, M. Morbidelli, Effect of shear rate on aggregate size and morphology investigated under turbulent conditions in stirred tank, Journal of Colloid and Interface Science 319 (2) (2008) 577–589.
[39] J.D. Boadway, Dynamic of growth and breakage of alum floc in presence of fluid shear, in: Proc. ASCE, J. Envir. Engng. Div., EE5, 104(5), 1978, pp. 901–915.
[40] R. Walden, R. Donnelly, Reemergent order of chaotic circular Couette flow, Physical Review Letters 42 (5) (1979) 301–304.
[41] R.C. DiPrima, P.M. Eagles, B.S. Ng, The effect of radius ratio on the stability of Couette flow and Taylor vortex flow, Physics of Fluids 27 (10) (1984) 2403–2411.
[42] K. Kataoka, Taylor Vortices and Instabilities in circular Couette flows, in: N.P. Cheremisinoff (Ed.), Encyclopaedia of Fluid Mechanics, vol. 1, Gulf Publishing, Houston, 1986, pp. 237–273.
[43] Y. Takeda, Quasi-periodic state and transition to turbulence in a rotating Couette system, Journal of Fluid Mechanics 389 (1) (1999) 81–99.
[44] L. Wang, D.L. Marchisio, R.D. Vigil, R.O. Fox, CFD simulation of aggregation and breakage processes in laminar Taylor–Couette flow, Journal of Colloid and Interface Science 282 (2) (2005) 380–396.
[45] L. Wang, M.G. Olsen, R.D. Vigil, Reappearance of azimuthal waves in turbulent Taylor–Couette flow at large aspect ratio, Chemical Engineering Science 60 (20) (2005) 5555–5568.
[46] M. Pivokonsky, R. Pivokonsky, L. Benesova, S. Mutl, Methodology of evaluation of size and size-distribution of particles formed during aggregation, Journal of Hydrology and Hydromechanics 51 (4) (2003) 281–287.
[47] Q. Jiang, B.E. Logan, Fractal dimensions of aggregates determined from steady state size distributions, Environmental Science and Technology 36 (4) (1991) 2031–2038.
[48] B. Gorczyca, J. Ganczarczyk, Structure and porosity of alum coagulation flocs, Water Quality Research Journal of Canada 34 (4) (1999) 653–666.
[49] N.H.G. Rahmani, T. Dabros, J.H. Masliyah, Fractal structure of asphaltene aggregates, Journal of Colloid and Interface Science 285 (2) (2005) 599–608.
[50] D.H. Li, J.J. Ganczarczyk, Fractal geometry of particles aggregates generated in water and wastewater treatment process, Environmental Science and Technology 23 (11) (1989) 1385–1389.
[51] P.T. Spicer, W. Keller, S.E. Pratsinis, The effect of impeller type on floc size and structure during shear-induced flocculation, Journal of Colloid and Interface Science 184 (1) (1996) 112–122.
[52] P. Meakin, Fractals, Scaling and Growth far from Equilibrium, Cambridge University Press, Cambridge, England, 1998.
[53] K.A. Kusters, J.G. Wijers, D. Thoenes, Aggregation kinetics of small particles in agitated vessels, Chemical Engineering Science 52 (1) (1997) 107–121.
[54] D.N. Thomas, S.J. Judd, N. Fawcett, Flocculation modelling: A review, Water Research 33 (7) (1999) 1579–1592.
[55] D.G. Lee, J.S. Bonner, L.S. Garton, A.N.S. Ernest, R.L. Autenrieth, Modeling coagulation kinetics incorporating fractal theories: a fractal rectilinear approach, Water Research 34 (7) (2000) 1987–2000.
[56] C. Selomulya, G.C. Bushell, R. Amal, D. Waite, Aggregation mechanisms of latex of different particle sizes in a controlled shear environment, Langmuir 18 (6) (2002) 1974–1984.

[57] J.J. Zhang, X.Y. Li, Modeling particle-size distribution dynamics in a flocculation system, AIChE Journal 49 (7) (2003) 1870–1882.
[58] M.C. Sterling, J.S. Bonner, A.N.S. Ernest, C.A. Page, R.L. Autenrieth, Application of fractal flocculation and vertical transport model to aquatic sol-sediment systems, Water Research 39 (9) (2005) 1818–1830.
[59] I. Reich, R.D. Vold, Flocculation–deflocculation in agitated suspensions, Journal of Physical Chemistry 63 (9) (1959) 1479–1501.
[60] K. Mühle, K. Domasch, Floc Strength in Bridging Flocculation, in: H.H. Hahn, R. Klute (Eds.), Chemical Water and Wastewater Treatment, Springer-Verlag, Berlin, 1990, pp. 105–115.
[61] F. Maggi, F. Mietta, J.C. Winterwerp, Effect of variable fractal dimension on the floc size distribution of suspended cohesive sediment, Journal of Hydrology 343 (1–2) (2007) 43–55.